Research Square

Preprints are preliminary reports that have not undergone peer review.
They should not be considered conclusive, used to inform clinical practice,
or referenced by the media as validated information.

Structural reorganization of mesoscale eddies amplifies global air-sea heat exchange

Peng Zhan

peng.zhan@kaust.edu.sa

Southern University of Science and Technology https://orcid.org/0000-0002-3996-7011

Gengbin Liu

Southern University of Science and Technology

Hongxing Cui

King Abdullah University of Science and Technology

Zhengguang Zhang

Ocean University of China https://orcid.org/0000-0001-9032-7629

Zhao Jing

Ocean University of China https://orcid.org/0000-0002-8430-9149

Shengpeng Wang

Ocean University of China

Article

Keywords:

Posted Date: April 23rd, 2026

DOI: https://doi.org/10.21203/rs.3.rs-9380272/v1

License: This work is licensed under a Creative Commons Attribution 4.0 International License. Read Full License

Additional Declarations: There is **NO** Competing Interest.

Structural reorganization of mesoscale eddies amplifies global air-sea heat exchange

Gengbin Liu[1], Hongxing Cui[2], Zhengguang Zhang[3,4], Zhao Jing[3,4], Shengpeng Wang[4], and Peng Zhan[1,2,*]

[1]Department of Ocean Science and Engineering, Southern University of Science and Technology, Shenzhen, Guangdong, China

[2]Physical Science and Engineering Division, King Abdullah University of Science and Technology, Thuwal, Saudi Arabia,

[3]Frontiers Science Center for Deep Ocean Multispheres and Earth System and Key Laboratory of Physical Oceanography/Academy of Future Ocean, Ocean University of China, Qingdao, China

[4]Laoshan Laboratory, Qingdao, China

*Corresponding author: P. Zhan (zhanp@sustech.edu.cn)

Abstracts

Mesoscale eddies are major regulators of air-sea heat exchange, yet their climatic impact has been assessed mainly through changes in eddy frequency or amplitude, implicitly assuming that the spatial organization of eddy-induced thermal anomalies is of secondary importance. Here, using 25 years of satellite observations, we show that mesoscale eddy impacts are increasingly shaped by a decadal-scale reorganization of their thermal structure. Globally, eddy-induced sea surface temperature anomalies are shifting toward more coherent, monopole-like configurations, increasing spatial coherence by about 4% per decade and raising by about 8% per decade the efficiency with which mesoscale heat-flux anomalies drive net air-sea exchange. A nonlinear attribution analysis shows that this transition arises from strengthened background SST gradients, enhanced eddy nonlinearity, and weakened relative air-sea thermal damping, with the strongest changes in western boundary current systems and the Southern Ocean. However, current high-resolution climate models fail to reproduce this observed shift, suggesting that mesoscale climate feedbacks may be underestimated. These results identify the structural evolution of mesoscale eddies as a previously unrecognized pathway through which climate warming amplifies air-sea heat exchange, with important implications for upper-ocean heat uptake and regional climate extremes.

Introduction

Mesoscale oceanic eddies are coherent vortices with horizontal scales of tens of hundreds of kilometers and account for a substantial fraction of the ocean's kinetic energy [1,2]. By stirring and trapping water masses and sharpening background temperature gradients, eddies play a fundamental role in redistributing heat, salt, and biogeochemical tracers throughout the global ocean [3-12]. Beyond their oceanic impacts, mesoscale eddies also interact strongly with the atmosphere. Through the generation of sea surface temperature anomalies (SSTAs), eddies can locally modulate turbulent air-sea heat fluxes and thereby influence the large-scale ocean-atmosphere energy balance [6,13-15]. Quantifying how eddies exchange heat with the atmosphere is therefore essential for understanding climate variability and its long-term evolution.

At the scale of individual eddies, anomalous air-sea turbulent heat fluxes are commonly conceptualized as a linear response to eddy-induced SSTAs, such that the surface heat flux anomaly $\overline{Q'}$ is proportional to the underlying temperature anomaly $\overline{T'}$, modulated by an air-sea thermal response rate k (i.e. $\overline{Q'} = k\overline{T'} + \varepsilon$) [16-18]. Recent study has reported a strengthening of this response rate over recent decades, largely associated with changes in large-scale sea surface temperature and its warming rate. These findings suggest that eddy-driven air-sea thermal coupling becomes increasingly efficient under a warming climate [16,19].

This theoretical framework, however, implicitly assumes that eddy-induced SSTAs are spatially homogeneous at the eddy scale, such that the eddy-averaged temperature anomaly adequately represents the thermal forcing experienced by the atmosphere. In reality, observations reveal pronounced diversity in the spatial organization of eddy-induced SSTAs [7,20-23]. While some eddies exhibit monopole-like temperature patterns with a coherent sign across the eddy core, others display more complex configurations, including dipole-like or strongly asymmetric structures. In such cases, positive and negative temperature anomalies may partially offset each other when averaged over the eddy, potentially reducing the effective thermal forcing despite comparable eddy intensity. This raises a fundamental and previously underexplored question: does the

internal structure of eddy-induced SSTAs regulate air-sea heat exchange? More specifically, can differences in SSTA structure systematically modulate the intensity of net air-sea heat flux associated with mesoscale eddies?

Beyond their instantaneous influence on air-sea heat exchange, an additional open question concerns whether eddy-induced SSTA structures themselves have evolved over time. Recent observational studies indicate that air-sea thermal coupling has undergone systematic changes under a warming climate, particularly in regions where mesoscale eddies exert a strong influence on ocean-atmosphere interactions [14,16,19]. In parallel, satellite observations reveal widespread changes in oceanic mesoscale kinetic energy, with significant strengthening of eddy activity reported across large portions of the global ocean [24-26]. Together, these changes raise the possibility that not only the intensity of eddies, but also the spatial structure of the SSTAs they induce, may be undergoing systematic evolution, with potential implications for the mesoscale air-sea heat exchange.

Here, we explicitly quantify how the spatial structure of eddy-induced SSTAs modulates eddy-scale net air-sea heat exchange and its variability at the global scale. Using established metrics that characterize SSTA structure and eddy-scale heat flux efficiency, we first diagnose the systematic evolution of eddy-induced SSTA structures over the satellite observations. Building on this diagnosed structural reorganization, we construct an interpretable machine-learning framework to identify the key derivers. The result demonstrates that eddy-induced SSTA structures are primarily sensitive to strengthening background SST gradients, increasing eddy nonlinearity, and weakening air-sea thermal damping, which are mechanistically connected to the dynamical controls associated with these drivers. This proposed framework closes the loop between observed structural evolution and physical mechanisms, enabling a quantitative assessment of the relative roles of various factors in shaping eddy-induced thermal structure and corresponding air-sea heat exchange under climate change.

Results

Global patterns of eddy-induced SSTA structure and associated heat flux signatures

We first examine the global distribution of eddy-induced SSTA structures using the structure index α (see Methods) following by Lv et al. (2022). The multi-year mean α filed exhibits pronounced spatial organization across the global ocean (Fig. 1a). Larger α values are preferentially found in mid-latitude regions and western boundary current systems, where strong background SST gradients and pronounced eddy nonlinearity favor coherent, monopole-like SSTA structures [4,26]. In contrast, smaller α values are more common in low-latitude regions and parts of the eastern ocean basins, consistent with previous findings that highlight enhanced structural asymmetry of eddy-induced SSTAs in these regions [20,22,23]. This spatial heterogeneity indicates that eddy-induced SSTA structure varies systematically across the global ocean.

This diversity in SSTA structures is clearly reflected in eddy-centered composites (Figs.1c-f). Anticyclonic and cyclonic eddies associated with large α values ($\alpha \geqslant 0.7$) exhibit coherent monopole-like SSTAs with a consistent sign across the eddy core (Figs. 1c-d). In contrast, eddies characterized by small α values ($\alpha \leqslant 0.3$) display pronounced dipole-like SSTA patterns, with adjacent regions of opposing anomalies within the eddy footprint (Figs. 1e-f). As a consequence, eddies of comparable spatial scale can impose markedly different eddy-averaged thermal forcings on the overlying atmosphere.

As the atmospheric adjustment to surface thermal anomalies occurs on timescales much shorter than the evolution of mesoscale eddies [27,28], these SSTA structural differences are directly imprinted onto the associated air-sea turbulent heat flux anomalies (HFAs). Monopole-like eddies exhibit HFAs that are spatially coherent and closely aligned with the underlying SSTAs (Figs. 1g-h), whereas dipole-like eddies are associated with HFAs of opposing sign within the eddy footprint (Figs. 1i-j). When

integrated over the eddy scale, these opposing contributions lead to substantial cancellation, resulting in a weak net heat exchange despite sizable local HFAs.

This spatial cancellation highlights a fundamental limitation of characterizing eddy-induced air-sea heat exchange using heat flux magnitude alone [29,30]. In dipole-like SSTA and HFA patterns, large HFAs can be largely cancelled spatially, yielding a weak net air-sea heat exchange, whereas more monopole-like structures can produce a stronger net exchange even with smaller amplitudes. As a result, metrics based solely on heat flux magnitude or spatial averaging cannot disentangle the relative roles of SSTA intensity and spatial organization. An efficiency-based description that explicitly accounts for the degree of cancellation is required. We thus quantify the net air-sea heat flux efficiency using the net ratio index η (see Methods), which measures the fraction of eddy-induced HFAs that effectively contributes to the net heat exchange. Consistent with the opposite thermal signatures of anticyclonic and cyclonic eddies, η is predominantly positive for anticyclonic eddies and negative for cyclonic eddies.

For clarity in presenting the global distribution, the sign of η for cyclonic eddies is reversed, such that larger values uniformly indicate higher efficiency of eddy-induced air-sea heat exchange regardless of eddy polarity. Under this convention, the global distribution of η exhibits coherent spatial patterns (Fig. 1b) that broadly mirror those of the SSTA structure index α, with particularly high values found in the central North Atlantic, central North Pacific and Southern Ocean ($\eta > 0.25$). To further assess the robustness of the structure-efficiency relationship, we examine five representative regions, including the Arabian Sea (AS), the Kuroshio Extension (KE), the Subtropical Countercurrent region (STCC), the Gulf Stream (GS), and the Antarctic Circumpolar Current (ACC), which encompass diverse dynamical regimes with active mesoscale and submesoscale eddy activity [4,31-33]. Across all regions, larger values of α are consistently associated with higher η (Fig. 1k), indicating that more monopole-like eddy-induced SSTA structures promote a more efficient net air-sea heat exchange.

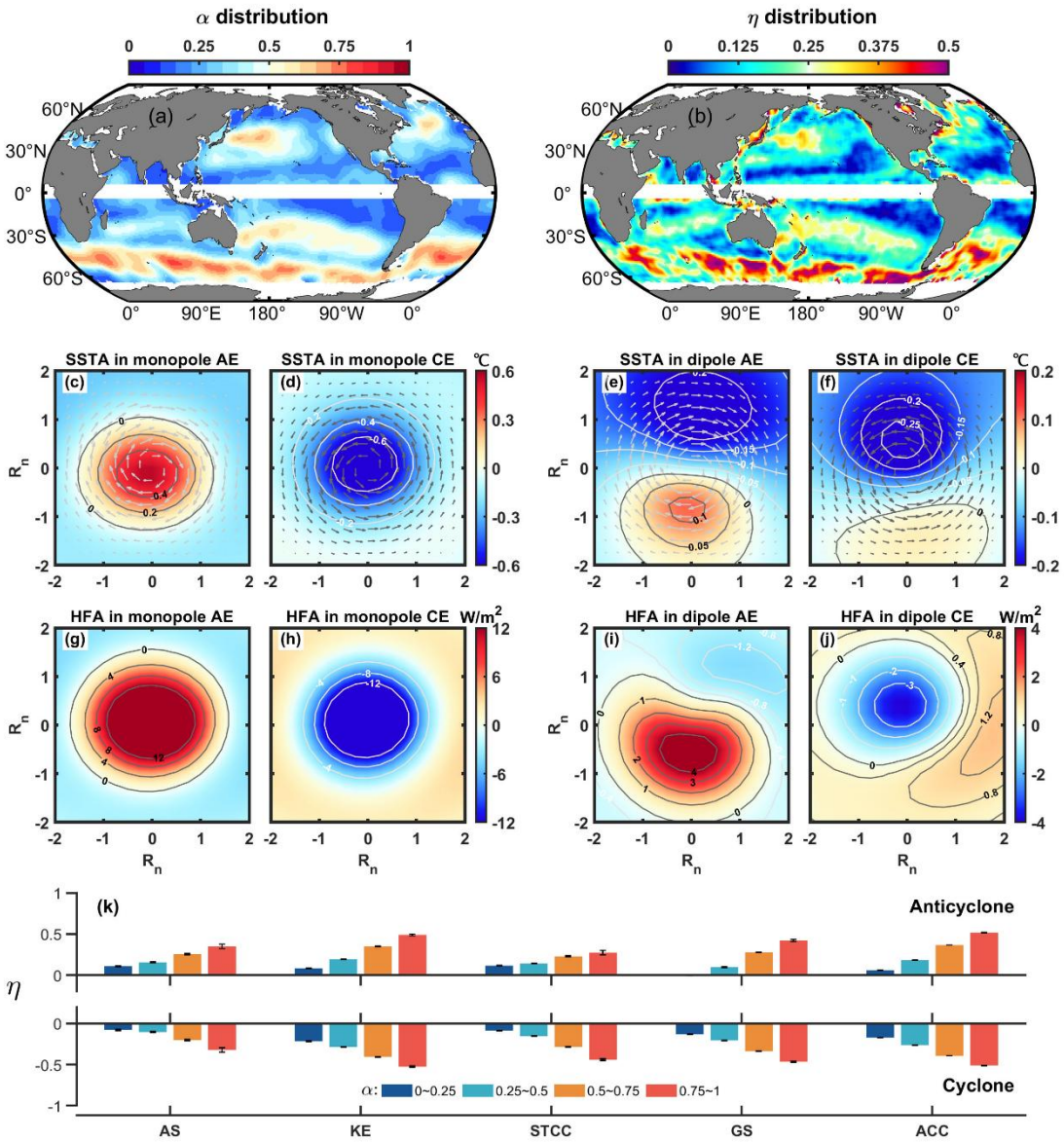


Fig 1. Global distribution of eddy-induced sea surface temperature anomaly (SSTA) structures and their associated air-sea heat exchange. (a) Spatial distribution of the eddy-induced SSTA structure index (α), which quantifies the degree of monopole-like organization in eddy-induced sea surface temperature anomalies. Values are calculated by aggregating all eddies occurring within each 1° × 1° grid box. (b) Climatological efficiency of air-sea heat exchange associated with eddy-induced SSTAs, quantified by the net ratio (η). The net ratio is defined as the ratio between the magnitude of the eddy-scale net turbulent heat flux anomaly and the spatial average of its absolute magnitude. For cyclonic eddies, negative values of η are shown as positive to facilitate comparison of efficiency. (c-f) Eddy-centered composites of eddy-induced SSTAs for monopole-dominated ($\alpha \geq 0.7$) and dipole-like ($\alpha \leq 0.3$)

anticyclonic eddies (AEs) and cyclonic eddies (CEs), shown in normalized eddy-radius coordinates R_n. (g-j) Corresponding composites of air-sea turbulent heat flux anomalies (HFA), including both sensible and latent heat flux components. (k) Regional dependence of air-sea heat exchange efficiency. Bars denote different α bins, representing increasing degrees of monopole-like SSTA structure. Upper and lower panels correspond to AEs and CEs, respectively. Black error bars indicate the 95% confidence intervals.

Long-term evolution of eddy-induced SSTA structure and air-sea heat exchange efficiency

To assess whether eddy-induced SSTA structures undergo systematic adjustments under a warming climate, we examine the long-term evolution of eddy-induced SSTA structure and the associated air-sea heat exchange efficiency using satellite observations from 1993 to 2018. Linear trends are estimated at each grid point based on 3-month averaged values, and their statistical significance is evaluated to assess the robustness of the inferred changes.

The global distribution of α trend exhibits a high degree of coherence, with predominantly positive values across much of the global ocean. The global-mean α increase at a rate of $(1.22 \pm 0.13) \times 10^{-2}$ per decade, corresponding to an approximate 4% per decade increase relative to its climatological mean (95% confidence level). However, pronounced regional contrasts are evident, with strong positive trends dominating the mid-latitude oceans, particularly in the Southern Ocean and downstream of major western boundary current systems. In contrast, trends in many low-latitude regions are weaker and often not statistically significant. These patterns indicate a widespread shift toward more monopole-like eddy-induced SSTA structures in dynamically energetic regimes, where strong eddy nonlinearity and background temperature gradients favor coherent thermal anomalies.

Trends in tropical regions are generally weaker and less robust. These regions are strongly influenced by internal climate variability, such as the El Niño-Southern Oscillation [34-36], which enhances interannual variability and reduces the detectability

of long-term trends in both eddy activity and the associated SSTA structures. Consistent with the weak or insignificant trends reported for eddy kinetic energy, the evolution of α in these regions lacks a clear long-term signal, suggesting the presence of multiple competing dynamical controls at low latitudes [24,26].

A broadly consistent pattern emerges for the long-term evolution of the net air-sea heat exchange efficiency η. Regions exhibiting significant positive trends in α are typically accompanied by increasing η, with a global-mean increase of $(1.19 \pm 0.22) \times 10^{-2}$ per decade (approximately 8% per decade). This correspondence indicates that the observed structural shift toward monopole-like SSTAs enhances the efficiency with which spatially distributed eddy-induced HFAs are converted into net air-sea heat exchange at the eddy scale. The linkage is particularly evident in the ACC and in the mid-latitude central North Atlantic and North Pacific.

Regional-mean time series further underscore the spatial heterogeneity of these trends (Fig. S1). In the KE, STCC, GS, and ACC regions, the SSTA structural index α exhibits statistically significant positive trends, increasing at rates of $(1.34 \pm 0.69) \times 10^{-2}$, $(7.06 \pm 3.09) \times 10^{-3}$, $(1.80 \pm 0.33) \times 10^{-2}$, and $(2.10 \pm 0.43) \times 10^{-2}$ per decade, respectively (all $p < 0.05$; Fig. 2c). These structural changes are accompanied by coherent and significant increases in the net air–sea heat flux efficiency η, with regional trends of $(1.44 \pm 1.13) \times 10^{-2}$ in the KE, $(1.06 \pm 1.02) \times 10^{-2}$ in the STCC, $(2.27 \pm 0.96) \times 10^{-2}$ in the GS, and $(2.02 \pm 0.04) \times 10^{-2}$ per decade in the ACC ($p < 0.05$; Fig. 2d). In contrast, both α and η exhibit weak and statistically insignificant trends in the AS, highlighting strong regional contrasts in the temporal evolution of eddy structure and air-sea heat exchange efficiency.

In addition, the long-term evolution of eddy-induced SSTA amplitude shows pronounced strengthening in mid-latitude regions, particularly within strong current systems (Fig. S2), consistent with previously reported increases in eddy intensity [24-26]. Taken together, these results suggest that mesoscale eddies may play an amplified role in air-sea heat exchange through two complementary pathways: a systematic shift toward more monopole-like SSTA structures and a concurrent intensification of SSTA amplitude. Both processes enhance the eddy-scale mean thermal forcing, which could

reinforce the contribution of mesoscale eddies to air-sea heat exchange in a warming climate.

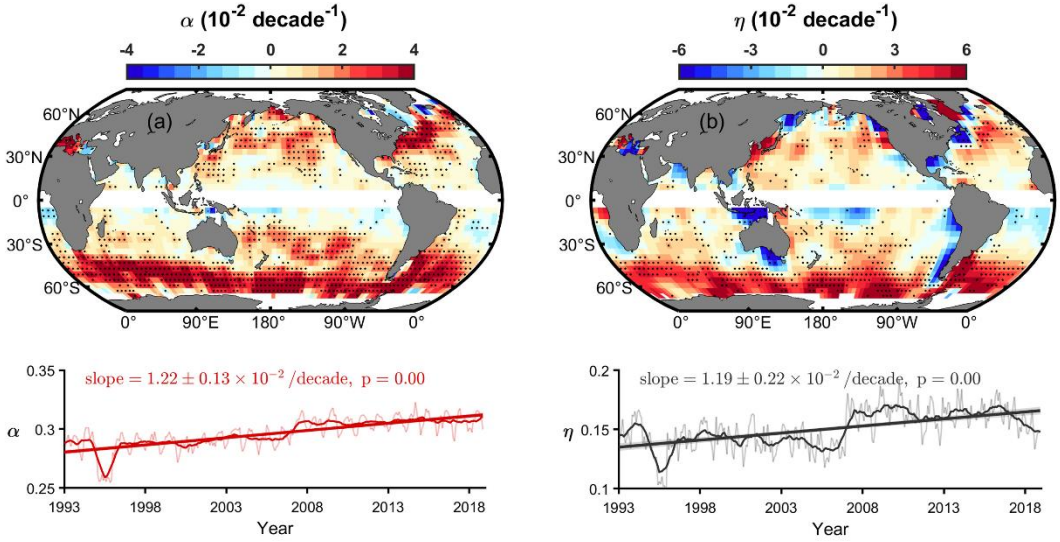


Fig 2. Long-term trends of eddy-induced sea surface temperature anomaly (SSTA) structure and air-sea heat flux net efficiency (η) from 1993 to 2018. (a) The global distribution of linear trends in the eddy-induced SSTA structure index (α) within each 4° × 4° grid box. Color denotes the trend magnitude ($\times 10^{-2}$ decade^{-1}), and black dots indicate grid point where the trend is statistically significant at the 95% confidence level. (b) Global distribution of linear trends in the air-sea heat flux net efficiency, quantified by the net ratio (η) over the same period. The low panels are regional time series of global averaged α and η. Thin lines represent the 3-month averaged, thick lines denote the annual average variations, and solid straight lines indicate linear trends with corresponding slopes and *p*-values. The shadow around the trend lines represents the 95% confidence intervals of the linear regression.

Modeling eddy-induced SSTA structure using explainable machine learning

Previous studies have discussed several dynamical processes that may shape eddy-induced SSTA structures in specific regions [7,22,23]. However, the key factors controlling SSTA structure at the global scale remain poorly constrained. To systematically identify the dominant controls on eddy-induced SSTA structure, we construct an interpretable

machine-learning framework combining Extreme Gradient Boosting (XGBoost; see Methods) and Shapley Additive exPlanations (SHAP; see Methods) to model and explain variations in the SSTA structural index α.

XGBoost is a powerful tree-based ensemble learning method that iteratively improves predictive skill by combining multiple weak learners into a strong predictor [37]. The model is trained using five physics-guided predictors, including the background SST gradient ($\nabla\overline{SST}$), latitude (Lat), eddy nonlinearity (U/c), normalized air-sea damping rate (λ^*) and background strain rate (SR_L). All predictor variables and the target α are spatially aggregated onto a common 2° × 2° grid and temporally averaged over 3-month periods, ensuring scale consistency between inputs and outputs. Based on an independent evaluation, the trained model achieves robust performance, with a correlation coefficient (r) of 0.70 between predicted and observed α values, a root-mean-square error (RMSE) of 0.07, and a mean absolute error (MAE) of 0.05 (Fig. 3a). These results indicate that the constructed model skillfully captures the cross-case variance in the observed α by considering these five physics-guided predictors.

To interpret how these predictors modulate the predicted structural index α, we employ SHAP to quantify the model sensitivity of α to individual predictors and to identify key drivers. SHAP is a post hoc interpretability approach that provides additive attributions for complex machine learning models [37-39]. For each sample, SHAP decomposes the prediction into baseline (the expected model output) plus the sum of individual feature contributions, i.e. $\hat{\alpha} = \boldsymbol{E}[\hat{\alpha}] + \sum_i \phi_i$, where ϕ_i represents the signed contribution of predictor i. In this study, positive (negative) SHAP values indicate that a predictor increases (decreases) the predicted α relative to the baseline.

To summarize the overall sensitivity, we use the mean absolute SHAP value across all samples, which measures the typical magnitude of a predictor influence on α and enables a robust ranking of dominant controls. This analysis indicates that the background SST gradient exerts the strongest control on α, followed by latitude, eddy nonlinearity and normalized air-sea damping rate (Fig. 3b). We further investigate the nonlinear relationships between α and the identified key drivers, as well as their global spatial distributions.

Specifically, the structural index α exhibits a nonlinear positive dependence on the background SST gradient (Fig. 3c). Positive SHAP values to α are predominantly associated with larger $\nabla\overline{SST}$ values, particularly exceeding $\sim 1.0 \times 10^{-5}$ ℃/m, beyond which a saturate effect emerges. This behavior suggests that strong background SST gradients promote the development of more monopole-like eddy-induced SSTA structures, while their influence saturates beyond a threshold value. As shown in previous studies [4,8,33], in regions characterized by strong horizontal SST gradients, eddies transport surface water masses across sharp thermal fronts, allowing same-sign temperature anomalies to accumulate within the eddy core over a given propagation distance or timescale. This accumulation promotes spatially coherent, monopole-like SSTA structures. By contrast, in regions with weak background SST gradients, the thermal contrast generated by eddy advection is inherently limited, rendering SSTAs more susceptible to subsequent air-sea thermal damping and lateral stirring, thereby inhibiting the development of high-α structures. Fig.3c also shows that large positive SHAP values associated with strong background SST gradients tend to co-occur with larger-amplitude SSTAs, consistent with the expectation that cross-front advection enhances the temperature contrast between the eddy interior and the surrounding environment. It should be noted that SSTA amplitude is shown as a diagnostic variable and is not included as a predictor in constructing the XGBoost model.

Fig. 3e displays that larger U/c values are generally associated with larger positive SHAP values, indicating more spatial coherent internal SSTA structures, particularly in highly nonlinear regimes ($U/c \geq 4$). This behavior is consistent with previous studies showing that stronger intrinsic nonlinearity, as indicated by larger U/c, implies a more dynamically constrained eddy core, enabling more effective retention and along-track advection of water masses during propagation [4,33]. Transport barriers at the eddy boundary play a critical role in suppressing lateral exchange. To quantitatively assess their presence and strength, we introduce finite-size Lyapunov exponents (FSLE) as an independent Lagrangian diagnostic that is not used in constructing the XGBoost model. As illustrated in Fig. 3e, large positive SHAP values associated with U/c preferentially occur in eddies exhibiting large FSLE edge-core

contrasts, indicating that the positive influence of eddy nonlinearity on α is most effective when strong boundary integrity is present. In contrast, eddies with weak FSLE contrasts tend to cluster around weak or even negative SHAP values, even at comparable U/c, reflecting enhanced lateral exchange and reduced internal structural coherence. In line with previous study [40-42], eddies with high α exhibit pronounced FSLE contrasts between the eddy periphery and core, indicative of strong transport barriers and weak lateral mixing, whereas dipole-like or asymmetric SSTA structures are associated with much weaker FSLE contrasts and enhanced exchange with surrounding waters (Fig. S3).

The normalized air-sea damping rate λ^* exerts an overall negative influence on α (Fig. 3f). As λ^* increases, atmospheric damping progressively suppresses the development and maintenance of coherent monopole-like SSTA structures, with a sharp reduction in predicted α once λ^* exceeds ~0.15. In this regime, air-sea heat exchange operates on timescales comparable to or shorter than eddy rotation, thereby efficiently damping eddy-induced SSTAs [23]. The suppressing role of thermal damping is particularly evident for eddies characterized by relatively weak SSTA amplitudes [27]. For such eddies, enhanced atmosphere heat feedback attenuates SSTAs within one or a few rotation periods, preventing the maintenance of coherent internal thermal structures. In contrast, eddies associated with stronger thermal anomalies exhibit greater resistance to atmospheric damping, allowing monopole-like SSTA configurations to persist despite ongoing air-sea heat exchange.

Although latitude emerges as the second important predictor, its influence primarily reflects the spatial organization and interaction of other key physical controls, rather than acting as an independent physical driver. In this sense, latitude serves as a large-scale modulator that integrates the combined effects of background SST gradients, eddy nonlinearity, and air-sea thermal damping, and its SHAP values reflect the spatial expression of these interacting processes. The latitudinal distribution of SHAP values exhibit systematically positive values at mid-to-high latitudes, with particularly strong signals in the Southern Hemisphere (Fig. S4). Importantly, these signals do not explicitly indicate stronger background conditions, but instead reflect enhanced SHAP

values associated with background SST gradients, eddy nonlinearity, and air-sea thermal damping. This pattern indicates that the influence of individual physical processes on the SSTA structural index α is amplified at these latitudes through their joint interaction, rather than acting independently. Overall, in regions where the SHAP values from $\nabla\overline{SST}$, U/c and λ^* are simultaneously elevated, thermal forcing, dynamical trapping, and atmospheric damping operate in a coordinated manner that favors the formation and maintenance of monopole-like SSTA structures. In particular, in the ACC and other strong current systems, λ^* is relatively weak [7,23,43]. Although surface heat fluxes in these regions can be substantial, rapid eddy dynamics redistribute and retain thermal anomalies before they are efficiently damped by the atmosphere, thereby enhancing the contribution of eddy-induced SSTAs to α. By contrast, at low latitudes, SHAP values from background SST gradients, eddy nonlinearity, and air-sea thermal damping are generally weak or compensating, reflecting a dynamical regime characterized by weak thermal gradients, reduced eddy nonlinearity, and strong air-sea thermal damping. Under such conditions, air-sea heat exchange operates on timescales comparable to or shorter than eddy rotation, efficiently eroding eddy-induced SSTAs and suppressing the development of high-α structures.

The pronounced hemispheric asymmetry in the latitudinal SHAP values further reflect fundamental differences in large-scale circulation geometry (Figs. 3d and S4b). In the Southern Hemisphere, continuous zonal flow and energetic circumpolar currents promote the formation of strong, spatially coherent nonlinear eddies [4,7,33], leading to systematically enhanced SHAP values of both dynamical and thermodynamic controls. In contrast, the fragmented basin geometry and multiple interacting jet systems in the Northern Hemisphere introduce substantial regional variability in eddy properties [22], weakening the systematic latitudinal organization of SHAP values and resulting in a less coherent dependence of α on latitude.

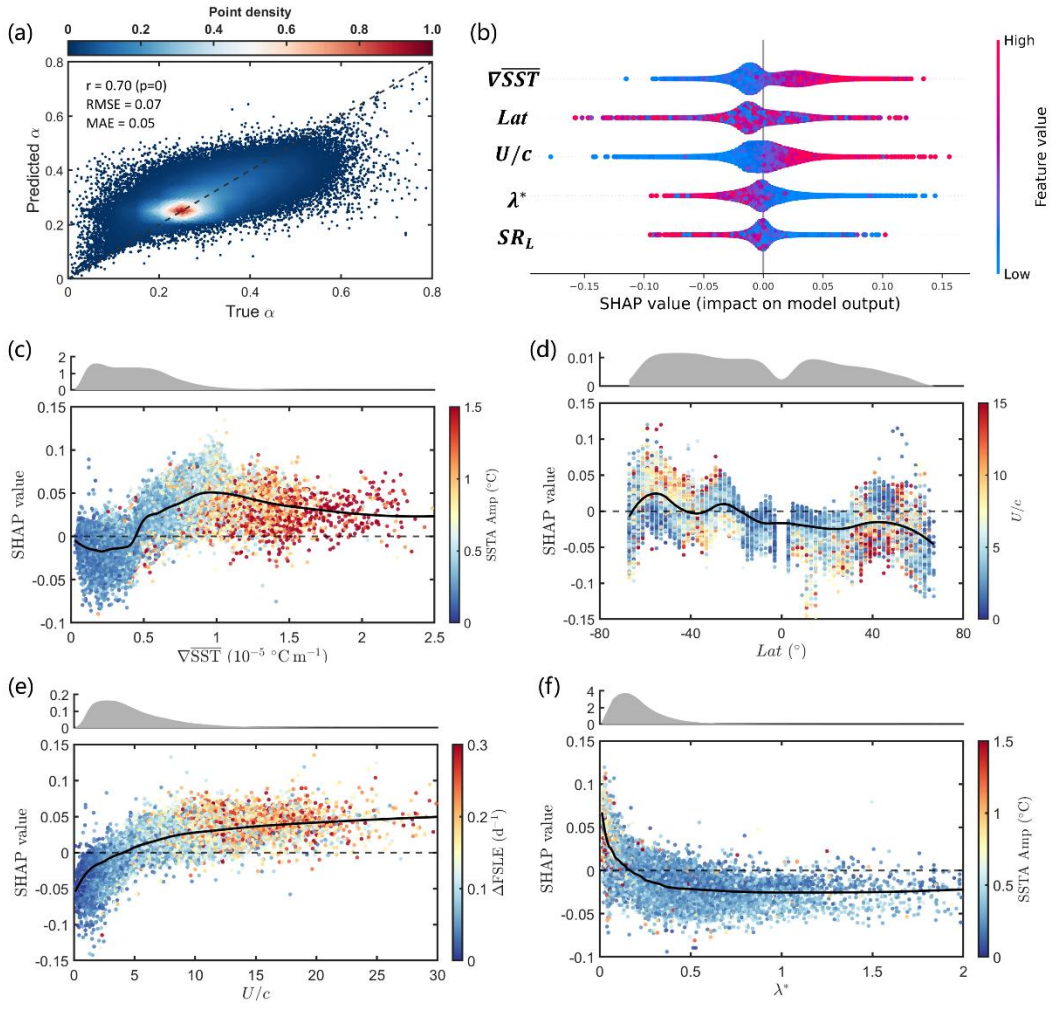


Fig 3. Model performance and SHAP-based interpretation of controls on the eddy-induced sea surface temperature anomaly (SSTA) structure index (α). (a) Scatter density plot of observed versus predicted α. Colors indicate point density, and statistical metrics (r, RMSE, MAE) quantify model performance. (b) SHAP summary plot of features ranked by the mean absolute SHAP value. SHAP values quantify the signed contribution of each predictor on the model prediction of α relative to a baseline (expected model output): positive (negative) SHAP values indicate that the predictor increases (decreases) the predicted α. Each point represents an individual sample, with colors indicating the corresponding feature value from low (blue) to high (red). (c-f) SHAP dependence plots for the four most important predictors. Colors represent the SSTA amplitude value in (c) and (f), eddy nonlinearity parameter (U/c) in (d), and the difference in finite-size Lyapunov exponent between the eddy edge and core ($\Delta FSLE$) in (e). Black curves denote locally smoothed trends. The grey shading in the top panel

shows the probability density function of the corresponding variable estimated using kernel density estimation. Note that SSTA amplitude and $\Delta FSLE$ are used here only for interoperation and are not included as predictors in the XGBoost model.

Interpreting trends in Eddy-induced SSTA structures

Motivated by the SHAP-based identification of the dominant controls on the eddy-induced SSTA structures, we further examine the long-term evolution of three leading factors to assess whether their observed trends are physically consistent with, and potentially help explain long-term changes in α.

At the global scale, both $\nabla\overline{SST}$ and U/c exhibit predominantly positive trends in the mid-latitude oceans, with most regions showing high statistical significance ($p < 0.05$), while trends in low-latitude regions are weaker and generally not significant (Figs. 4a-b). These patterns are consistent with previous satellite-based studies reporting a strengthening of mesoscale eddy activity and eddy kinetic energy in the extratropical oceans [25,26]. In contrast, λ^* displays a robust negative trend across much of the global ocean, with particularly strong and statistically significant decreases in mid- to high-latitude regions. This spatially coherent decline indicates a systematic shift in the relative balance between atmospheric thermal damping and eddy rotational timescales over the satellite era. Taken together, these trends suggest that over large portions of the extratropical ocean, the thermal and dynamical environment has evolved in a manner increasingly favorable for the formation and persistence of monopole-like SSTAs, consistent with the observed increase in α in these regions.

To further examine how these global-scale trends manifest regionally, we next focus on three representative mid-to-high latitude regions: KE, GS, and ACC. These regions exhibit some of the strongest and most statistically significant long-term increases in α and are characterized by intense mesoscale activity, making them well suited for regional-scale attribution of the underlying physical drivers.

In the KE region, significant positive trends in both $\nabla\overline{SST}$ ($p = 0.03$) and U/c ($p = 0.02$) are observed, while changes in λ^* are comparatively weak (Figs. 4d-f). This

pattern indicates that the strengthening of background thermal gradients and enhanced eddy nonlinearity jointly underpin the pronounced increase in α observed there. In the GS region, $\nabla\overline{SST}$ exhibits a robust and statistically significant increase (p = 0.00), reflecting a strengthening of the large-scale thermal contrast (Fig. 4g). By contrast, the regional-mean trend in U/c is not statistically significant (p = 0.34, Fig. 4h), primarily because its spatial pattern is characterized by pronounced sign reversals within the region, leading to substantial cancellation upon regional averaging. In addition, λ^* shows only weak temporal variations in this region, resulting in an insignificant regional-mean trend (p = 0.13, Fig. 4i). These results indicate that, at the regional scale, changes in eddy-induced SSTA structure in the GS are primarily associated with the evolution of the background SST gradient, while contributions from eddy nonlinearity and air-sea damping remain secondary.

The ACC region exhibits the most coherent and synergistic signal among the three factors. Here, $\nabla\overline{SST}$ and U/c increase significantly, while λ^* decreases robustly, indicating concurrent strengthening of thermal forcing and eddy trapping alongside a weakening of air-sea thermal damping (Figs. 4j-l). This coordinated evolution closely corresponds to the strong and spatially coherent increase in α observed in the Southern Ocean, where energetic and nonlinear eddies dominate the mesoscale circulation [4,25,33].

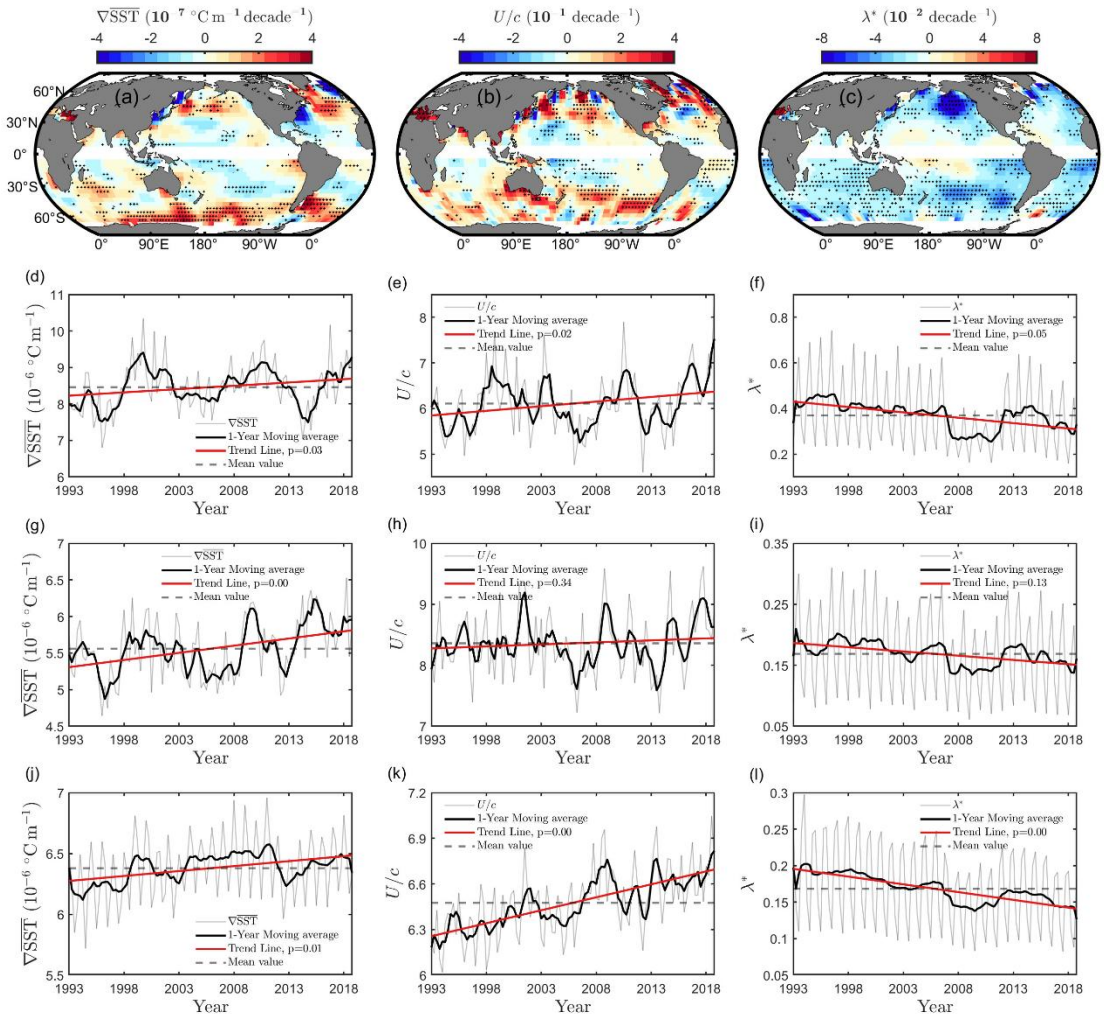


Fig 4. Interannual variability and long-term trends of key physical factors controlling the eddy-induced sea surface temperature (SSTA) structure. (a-c) Spatial distribution of the linear trend (1993-2018) in the background sea surface temperature gradient ($\nabla\overline{SST}$), the eddy nonlinearity parameter (U/c), and the normalized air-sea damping rate (λ^*) within $4^\circ \times 4^\circ$ grid boxes, respectively. Black dots indicate grid points where the trend is statistically significant at the 95% confidence level. (d-f) Regional-mean interannual time series and linear trends of $\nabla\overline{SST}$, U/c and λ^* in the Kuroshio Extension (KE) region. (g-i) As in (d-f), but for the Gulf Stream (GS) region. (j-l) As in (d-f), but for the Antarctic Circumpolar Current (ACC) region.

Discussion

Mesoscale eddies play a key role in regulating local air-sea heat exchange and have attracted increasing attention in the context of climate change. Our findings reveal

that the climatic impact of mesoscale ocean eddies is governed by a fundamental, decadal-scale reorganization of their thermal structure. Historically, mesoscale air-sea interaction has been evaluated through linear feedback frameworks that treat eddy-induced SSTAs as spatially homogeneous. While these models capture the strengthening of thermal coupling driven by rising temperatures, they inadvertently mask the vital role of internal spatial organization. Our discovery of a systematic global trend toward monopole-like SSTA configurations challenges this simplification. Crucially, this mechanism operates even in regions where changes in SSTA amplitude are modest (Fig. S2), highlighting that structural evolution alone can substantially modulate the global energy budget. In high-energy regimes, such as the Southern Ocean and western boundary currents, where structural coherence and SSTA amplitudes are increasing concurrently, the mesoscale contribution to air-sea heat exchange is being amplified through a synergistic process. This dual amplification, through both enhanced thermal anomalies and more efficient structural organization, underscores the growing importance of mesoscale processes in shaping local ocean-atmosphere interactions under warming conditions.

The physical drivers of this reorganization, identified through an explainable, data-driven framework that captures complex, nonlinear relationships more flexibly and accurately, underscore a synergistic response to environmental shifts. The transition to monopole-like structures is primarily driven by strengthening background SST gradients, increasing eddy nonlinearity, and a relative weakening of atmospheric thermal damping. These factors operate in a coordinated manner to enhance the trapping and retention of thermal anomalies within eddy cores. While the current observational record is limited to approximate three decades, the mechanisms identified suggest that these structural changes are likely a manifestation of broader climate change. This structural intensification implies that the mesoscale ocean is an active participant regulating the efficiency of the global energy budget through its evolving geometry.

The implications for our understanding of the Earth system are promising. If these structural shifts are not accounted for, we risk systematically underestimating the

magnitude and pace of mesoscale climate feedbacks. Enhanced eddy-scale heat exchange efficiency implies that mesoscale processes contribute more effectively to local variability than previously assumed. This amplification has the potential to strengthen upper-ocean temperature anomalies, thereby increasing the risk of regional climate extremes such as marine heatwaves or the rapid intensification of tropical cyclones. By facilitating a more efficient transfer of heat between the ocean and the atmosphere, this structural reorganization may partially offset the observed decline in large-scale air-sea heat exchange efficiency [(44)], effectively shifting the burden of ocean-atmosphere coupling to the mesoscale.

Critically, this structural evolution represents a previously unrecognized pathway for climate feedback, which is complementary to changes in eddy amplitude and background mesoscale air-sea coupling. The failure of state-of-the-art climate models to replicate this observed shift in SSTA structure points to a gap in current climate predictability. This discrepancy likely reflects limitations in the representation of mesoscale dynamics and their response to changing background states, specifically regarding the maintenance of eddy nonlinearity and the resolution of sharp thermal gradients (Fig. S5). Without accounting for the evolving thermal architecture of the mesoscale ocean, climate projections remain incomplete. Our results therefore serve as a call to action for the modeling community. To achieve high-fidelity climate projections and accurate assessments of regional risk, we shall move beyond intensity-based metrics and resolve the dynamic structural reorganization that is reshaping the ocean's thermal influence on the global climate.

Methods

Eddy Tracking Data Set and Satellite Altimetry

Mesoscale eddy properties, including eddy location, radius, spatial extent, lifetime, shape, and trajectory over the period 1993-2018, were obtained from the Global Ocean Mesoscale Eddy Atmospheric-Oceanic-Biological Interaction Observational Dataset

(GOMEAD) [45]. GOMEAD is constructed using a velocity-vector-geometry-based eddy detection algorithm [46] and includes only eddies with lifetimes exceeding four weeks. Because this detection approach relies on the geometric characteristics of the velocity field, GOMEAD does not provide direct estimates of eddy amplitude or maximum azimuthal velocity.

To supplement this limitation, satellite altimetry products from the Copernicus Climate Change Service (C3S), processed and distributed by the SSALTO/DUACS system, were employed. The altimetry data have a daily temporal resolution and a horizontal spacing of 0.25°, and provide sea level anomaly (SLA), geostrophic velocity, and geostrophic velocity anomalies (u_a, v_a) for the period 1993-2018.

Because the GOMEAD dataset does not report the maximum azimuthal velocity of individual eddies, each eddy was further characterized using the geostrophic velocity anomaly field derived from satellite altimetry. For each time step, the eddy center was refined by recentering it according to the local velocity structure to ensure consistency with the geostrophic flow. The maximum azimuthal velocity U was estimated as the mean geostrophic speed of the upper 90% of values within one eddy radius, which provides a robust measure of eddy intensity while reducing sensitivity to local noise. The eddy translation speed c was calculated from the displacement of the eddy center between consecutive time steps along each eddy trajectory. The degree of eddy nonlinearity was subsequently quantified using the standard nondimensional parameter U/c, which characterizes the ability of an eddy to trap and retain fluid within its core.

To quantify the influence of the large-scale background strain on the structure of eddy-induced sea surface temperature anomalies (SSTAs), the background geostrophic flow was extracted by applying a Gaussian low-pass spatial filter with a 10°×10° window to the geostrophic velocity field. The filtered velocity field, denoted as (u_L, v_L), represents the large-scale background circulation with mesoscale variability removed. Based on this background flow, the large-scale strain rate SR_L was calculated as

$$SR_L = \sqrt{(\frac{\partial u_L}{\partial x} - \frac{\partial v_L}{\partial y})^2 + (\frac{\partial v_L}{\partial x} + \frac{\partial u_L}{\partial y})^2}. \quad (1)$$

Eddy-induced Sea Surface Temperature Anomaly and structural Characterization

To characterize the thermodynamic imprint of mesoscale eddies on the sea surface temperature field, we first constructed eddy-induced SSTAs and their composite structures, and subsequently quantified their structural characteristics using a previously proposed structural index α.

Daily sea surface temperature (SST) data were obtained from the Optimum Interpolation Sea Surface Temperature (OISST) dataset (version 2.1) provided by NOAA/NESDIS/NCEI, with a horizontal resolution of 0.25°×0.25° over the period 1993-2018. The OISST product is primarily derived from Advanced Very High Resolution Radiometer (AVHRR) observations and incorporates in situ ship and buoy measurements to correct satellite biases [47,48]. To separate eddy-scale temperature anomalies from the large-scale background SST field, a Gaussian spatial filter with a $10° \times 10°$ characteristic scale was applied to the daily SST data. The high-pass component of the filtered field represents eddy-induced SSTAs (T'), while the corresponding low-pass component defines the large-scale background SST field $\bar{T}$. This scale separation allows mesoscale eddy signals to be consistently distinguished from the slowly varying background thermal field. The background SST gradient was then calculated from the low-pass SST field as

$$\nabla\overline{SST} = \sqrt{\left(\frac{\partial \bar{T}_x}{\partial x}\right)^2 + \left(\frac{\partial \bar{T}_y}{\partial x}\right)^2}. \quad (2)$$

For each detected eddy, eddy-centered SSTA snapshots were extracted following a unified procedure. The zonal and meridional gradients of the climatological monthly mean SST derived from the World Ocean Atlas 2023 (WOA23), denoted as $\overline{SST}_{mx}$ and $\overline{SST}_{my}$, were first computed and interpolated to the instantaneous eddy center. The orientation of the background SST gradient was defined by the azimuth angle

$$\theta = tan^{-1}\left(\frac{\overline{SST}_{my}}{\overline{SST}_{mx}}\right). \quad (3)$$

To place all eddies within a common thermodynamic reference frame, the background SST gradient direction at the eddy center was aligned with a reference polar

angle of 90°. An eddy-centered SSTA snapshot covering a 4°×4° domain was then extracted. The original eddy-centric coordinates (x, y) were rotated according to the background gradient direction,

$$\begin{pmatrix} x_n \\ y_n \end{pmatrix} = \begin{pmatrix} sin\theta & \cos\theta \\ -cos\theta & \sin\theta \end{pmatrix} \begin{pmatrix} x \\ y \end{pmatrix}. \quad (4)$$

and subsequently normalized by the corresponding eddy radius R.

All normalized eddy-centered SSTA snapshots were then aggregated to obtain composite SSTA structures. To ensure consistency between hemispheres, eddy snapshots in the Southern Hemisphere were first flipped meridionally and subsequently rotated by 180°, such that their orientation was aligned with those in the Northern Hemisphere. Subregional and global composite SSTA patterns were finally obtained by averaging all aligned snapshots, representing the climatological mean thermodynamic imprint of mesoscale eddies under different background conditions.

To further quantify the structural characteristics of eddy-induced SSTA, we adopted a structural index α following Lv et al. (2022). The index is defined as the Pearson correlation coefficient between the original eddy-induced SSTA field and its radially mean field (T_{rm}) as

$$\alpha = R(T', T_{rm}). \quad (5)$$

The structural index α quantifies the extent to which an eddy-induced SSTA pattern resembles an idealized axisymmetric monopole structure. Larger α values indicate more coherent, monopole-like SSTAs, whereas smaller values correspond to increasingly distorted or dipole-like configurations. The index α was calculated for individual eddies to characterize the instantaneous thermodynamic imprint of each eddy under its local background environment, thereby capturing the diversity and variability of eddy-induced SSTA structures.

Turbulent Air-sea Heat Flux Anomalies and damping rate

To further evaluate the impact of mesoscale air-sea interaction, we used the daily surface turbulent heat flux datasets (version 4.1) distributed by the Institute Français de Recherche pour l'Exploitation de la Mer (IFREMER) from 1993 to 2018, with spatial

resolution of 0.25°. The datasets contain sensible heat (Q_s), latent heat (Q_L) and associated bulk variables.

To ensure consistency with the extraction of eddy-induced SSTA, turbulent heat flux anomalies were computed using the same spatial filtering procedure applied to the SST field. Specifically, a Gaussian spatial filter was used to remove large-scale background variability from the sensible and latent heat flux fields, yielding sensible heat anomaly (Q_s') and latent heat anomaly (Q_L'). These anomalies primarily represent the modulation of turbulent air-sea heat exchange associated with mesoscale eddies. For each detected eddy, eddy-centered heat flux anomaly snapshots were extracted following the same eddy-centered coordinate system used for SSTA. This ensured a consistent spatial alignment between SSTA patterns and the corresponding turbulent heat flux anomalies. To quantify the degree to which spatially heterogeneous heat flux anomalies contribute to a net air-sea heat exchange, we defined a net ratio index,

$$\eta = \frac{\overline{Q'}}{\overline{|Q'|}}. \tag{6}$$

where Q' denotes the total turbulent heat flux anomaly ($Q' = Q_s' + Q_L'$), and the overbar represents spatial averaging over the eddy domain within $1.5R$. The net ratio index provides a measure of the spatial cancellation of heat flux anomalies within an eddy, with larger values indicating a more spatially coherent heat flux pattern.

To characterize the thermodynamic feedback of turbulent heat fluxes on eddy-induced SSTAs, we estimated the local linear response rates of sensible and latent heat flux anomalies to SSTAs for each eddy. The response rates were calculated using least-squares linear regression,

$$R_S = \frac{\partial Q_S'}{\partial T'}, \tag{7}$$

$$R_L = \frac{\partial Q_L'}{\partial T'}. \tag{8}$$

The combined effect of sensible and latent heat flux feedbacks is represented by a damping rate,

$$\lambda = \frac{R_S + R_L}{\rho_0 c_p H}, \tag{9}$$

where ρ_0 is the reference seawater density (1025 kg/m^3), c_p is the specific heat

599 capacity of seawater (4,000 J kg^{-1} K^{-1}), and H is the climatological mixed-layer depth.
600 The mixed-layer depth was estimated from Argo hydrographic profiles using a density-
601 threshold method [49].

602 The damping rate was further normalized by the eddy stirring timescale ($\frac{U}{2\pi R}$),
603 yielding a nondimensional normalized damping rate that allows comparison across
604 eddies with different sizes and intensities.

605 $$\lambda^* = \frac{2\pi R\lambda}{U}. \quad (10)$$

606 ## Lagrangian Coherent Structure

607 The finite-size Lyapunov exponents (FSLE) calculated by the Archiving, Validation,
608 and Interpretation of Satellite Oceanographic data (AVISO) were also used to quantify
609 oceanic stirring and mixing over 1993-2018, which a horizontal spacing of 1/25°. FSLE
610 is a Lagrangian diagnostic that measures the exponential rate at which pairs of fluid
611 particles separate from an initial distance to a prescribed final distance, and thus
612 provides a quantitative estimate of the local stretching and filamentation of water
613 masses [40,41,50]. In this study, regions with high FSLE values are interpreted as areas of
614 intense mesoscale stirring, which allows us to assess how mesoscale eddies regulate the
615 exchange of water masses between the eddy interior and the surrounding flow.

616 ## Explainable Machine Learning Framework

617 To investigate the factors controlling eddy-induced SSTA structures, we constructed
618 an interpretable machine-learning framework to quantify the relationships between
619 multiple environmental predictors and the SSTA structural index α. The framework
620 consists of two components: a predictive model based on eXtreme Gradient Boosting
621 (XGBoost) and a post hoc interpretability analysis using SHapley Additive
622 exPlanations (SHAP).

623 XGBoost is an ensemble, tree-based regression method that constructs a predictive
624 model by sequentially combining multiple decision trees [37,38]. This approach has been
625 successfully applied in for a range of geophysical applications [51-53] because it is skillful

at capturing nonlinear relationships, threshold behavior, and interactions among predictors. In addition, XGBoost is relatively robust to differences in variable scaling and to collinearity among predictors, which are common features in multivariate oceanographic datasets [38,54]. In this study, XGBoost was used to model the relationship between physics-guided variables (i.e., $\nabla\overline{SST}$, U/c, λ^*, *Lat*, and SR_L) and the eddy-induced SSTA structural index α. At each boosting iteration t, the model prediction for the i-th eddy is expressed as the sum of individual tree contributions,

$$\hat{y}_i^t = \sum_{k=1}^{t} f_k(x_i) = \hat{y}_i^{t-1} + f_t(x_i), \tag{11}$$

where x_i denotes the predictor vector for eddy i, and f_t represents the decisions tree added at iteration t. The tree structure and parameters are determined by minimizing an objective function that balances model fit and complexity,

$$Obj^t = \sum_{i=1}^{n} L(y_i, \hat{y}_i^{t-1} + f_t(x_i)) + \omega^t. \tag{12}$$

Here, $L(y_i, \hat{y}_i^{t-1} + f_t(x_i))$ is a loss function measuring the mismatch between predicted and observed values; $\omega^t = \sum_{k=1}^{t} \omega(f_i)$ is a regularization term that penalizes overly complex trees; $\omega(f_i)$ is defined as $\gamma T^i + \frac{1}{2}\lambda\left\|\xi^i\right\|^2$; γ represents the regularization term that penalizes the number of leaves, T^i in the tree, and; λ is the regularization term that the weights ξ^i assigned to different leaves.

The obtained dataset is randomly partitioned into two subsets, with 80% of the samples used for model training and the remaining 20% reserved for performance evaluation. The training subset is employed to determine the optimal hyperparameters through a trial-and-error approach and to obtain the trained model. The independent evaluation subset is then used to assess the performance of the final trained model. Detailed descriptions of the hyperparameter optimization procedures are provided in Text S1 of Supporting Information S1.

To interpret the trained XGBoost model and quantify the contribution of individual predictors to the predicted SSTA structure, we applied the SHAP method. SHAP is a game-theory-based approach that decomposes a model prediction into additive contributions from each predictor by considering all possible combinations of features [39]. This property ensures a consistent and physically interpretable attribution of feature

importance. For each eddy instance, the model prediction can be expressed as

$$\hat{\alpha}_i = \alpha_{base} + \sum_{j=1}^{m} \phi_{ij}, \quad (13)$$

where α_{base} is the baseline prediction (typically, the mean predicted SSTA structure across all instances), ϕ_{ij} is the SHAP value associated with the j-th predictor for the i-th eddy, and m is the number of predictors. The SHAP value ϕ_{ij} represents the contribution of predictors j to the deviation of the predicted structural index from the baseline. Positive SHAP values indicate that a given predictor promotes a more monopole-like SSTA structure (larger α), whereas negative SHAP values indicate a tendency toward more distorted or dipole-like structures. By analyzing the distribution of SHAP values across all eddies, this approach allows both the relative importance of different physical factors and the directionality of their effects on SSTA structure to be quantified in a physically interpretable manner.

Acknowledgments: This work was supported by Shenzhen Science and Technology Program (JCYJ20240813094213018) and KAUST's CompetitiveResearchGrants (URF/1/6419-01-01).

Author contribution: G. L. carried out the data analysis. H. C. constructed the explainable machine learning framework. G. L. and P. Z. conceived of the initial idea. Z. Z. and Z. J. helped with conceptualization and interpretation. W. S provided the data about high-resolution climate model. All authors contributed to the research question, revisions, and writing of the manuscript.

Competing interests: The authors declare that they have no competing interests.

Data availability

The Eddy-tracking dataset can be accessed at https://doi.org/10.11922/sciencedb.01190. The satellite altimetry products are available at https://cds.climate.copernicus.eu. The daily NOAA OISST v2.1 data are available at https://www.ncei.noaa.gov/data/sea-surface-temperature-optimum-interpolation/v2.1/access/avhrr/. The daily surface turbulent heat flux datasets are available at https://data-cersat.ifremer.fr/data/heat-

flux/esa-oceanheatflux/data/oceanheatflux/turbulent-fluxes/full-series/. The finite-size Lyapunov exponents (FSLE) products are available at https://www.aviso.altimetry.fr/en/data/products/value-added-products/fsle-finite-size-lyapunov-exponents.html. The mixed-layer depth dataset is obtained from http://mixedlayer.ucsd.edu. The World Ocean Atlas (WOA23) dataset is available at https://www.ncei.noaa.gov/access/world-ocean-atlas-2023/.

Reference:

1. Wunsch C. & Ferrari R. Vertical Mixing, Energy, and the General Circulation of the Oceans. *Annu. Rev. Fluid Mech.* **36**, 281-314 (2004).
2. Ferrari R. & Wunsch C. Ocean Circulation Kinetic Energy: Reservoirs, Sources, and Sinks. *Annu. Rev. Fluid Mech.* **41**, 253-282 (2009).
3. Amores A., Melnichenko O. & Maximenko N. Coherent mesoscale eddies in the North Atlantic subtropical gyre: 3-D structure and transport with application to the salinity maximum. *J. Geophys. Res.: Oceans* **122**, 23-41 (2017).
4. Chelton D. B., Schlax M. G. & Samelson R. M. Global observations of nonlinear mesoscale eddies. *Prog. Oceanogr.* **91**, 167-216 (2011).
5. Du T., Jing Z., Wu L., Wang H., Chen Z., Ma X., Gan B. & Yang H. Growth of ocean thermal energy conversion resources under greenhouse warming regulated by oceanic eddies. *Nat Commun* **13**, 7249 (2022).
6. Frenger I., Gruber N., Knutti R. & Münnich M. Imprint of Southern Ocean eddies on winds, clouds and rainfall. *Nat. Geosci.* **6**, 608-612 (2013).
7. Frenger I., Münnich M., Gruber N. & Knutti R. Southern Ocean eddy phenomenology. *J. Geophys. Res.: Oceans* **120**, 7413-7449 (2015).
8. He Q., Zhan W., Cai S., Du Y., Chen Z., Tang S. & Zhan H. Enhancing impacts of mesoscale eddies on Southern Ocean temperature variability and extremes. *Proc Natl Acad Sci U S A* **120**, e2302292120 (2023).
9. He Q., Zhan W., Feng M., Gong Y., Cai S. & Zhan H. Common occurrences of subsurface heatwaves and cold spells in ocean eddies. *Nature* **634**, 1111-1117 (2024).
10. Wang H., Qiu B., Liu H. & Zhang Z. Doubling of surface oceanic meridional heat transport by non-symmetry of mesoscale eddies. *Nat Commun* **14**, 5460 (2023).
11. Yuan Q., Zhang Z., Liu T., Zhao W. & Tian J. Stirring by mesoscale eddies dominates meridional eddy heat transport in global ocean. *Sci. China Earth Sci.* **68**, 2904-2912 (2025).

12. Zhan P., Krokos G., Guo D. & Hoteit I. Three-Dimensional Signature of the Red Sea Eddies and Eddy-Induced Transport. *Geophys. Res. Lett.* **46**, 2167-2177 (2019).
13. Leyba I. M., Saraceno M. & Solman S. A. Air-sea heat fluxes associated to mesoscale eddies in the Southwestern Atlantic Ocean and their dependence on different regional conditions. *Clim. Dyn.* **49**, 2491-2501 (2016).
14. Ma X., Jing Z., Chang P., Liu X., Montuoro R., Small R. J., Bryan F. O., Greatbatch R. J., Brandt P., Wu D., Lin X. & Wu L. Western boundary currents regulated by interaction between ocean eddies and the atmosphere. *Nature* **535**, 533-537 (2016).
15. Moreton S., Ferreira D., Roberts M. & Hewitt H. Air-Sea Turbulent Heat Flux Feedback Over Mesoscale Eddies. *Geophys. Res. Lett.* **48** (2021).
16. Ma X., Zhang X., Wu L., Tang Z., Yang P., Song F., Jing Z., Chen H., Qu Y., Yuan M., Chen Z. & Gan B. Midlatitude mesoscale thermal Air-sea interaction enhanced by greenhouse warming. *Nat Commun* **15**, 7699 (2024).
17. Yang P., Jing Z. & Wu L. An Assessment of Representation of Oceanic Mesoscale Eddy-Atmosphere Interaction in the Current Generation of General Circulation Models and Reanalyses. *Geophys. Res. Lett.* **45** (2018).
18. Yuan M., Li F., Ma X. & Yang P. Spatio-temporal variability of surface turbulent heat flux feedback for mesoscale sea surface temperature anomaly in the global ocean. *Front. Mar. Sci.* **9** (2022).
19. Tong J., Song X., Jiang W. & Cai W. Enhanced Wintertime Surface Heat Flux Feedback in the North Pacific Over Six Recent Decades. *Geophys. Res. Lett.* **52** (2025).
20. Gaube P., Chelton D. B., Samelson R. M., Schlax M. G. & O'Neill L. W. Satellite Observations of Mesoscale Eddy-Induced Ekman Pumping. *J. Phys. Oceanogr.* **45**, 104-132 (2015).
21. Hausmann U. & Czaja A. The observed signature of mesoscale eddies in sea surface temperature and the associated heat transport. *Deep Sea Res. Part I* **70**, 60-72 (2012).
22. Lv M., Wang F., Li Y., Zhang Z. & Zhu Y. Structure of Sea Surface Temperature Anomaly Induced by Mesoscale Eddies in the North Pacific Ocean. *J. Geophys. Res.: Oceans* **127** (2022).
23. Wu W. & Mahadevan A. Air-Sea Turbulent Heat Flux Affects Oceanic Lateral Eddy Heat Transport. *Geophys. Res. Lett.* **51** (2024).
24. Beech N., Rackow T., Semmler T., Danilov S., Wang Q. & Jung T. Long-term evolution of ocean eddy activity in a warming world. *Nat. Clim. Change* **12**, 910-917 (2022).
25. Hogg A. M., Meredith M. P., Chambers D. P., Abrahamsen E. P., Hughes C. W.

& Morrison A. K. Recent trends in the Southern Ocean eddy field. *J. Geophys. Res.: Oceans* **120**, 257-267 (2015).
26. Martínez-Moreno J., Hogg A. M., England M. H., Constantinou N. C., Kiss A. E. & Morrison A. K. Global changes in oceanic mesoscale currents over the satellite altimetry record. *Nat. Clim. Change* **11**, 397-403 (2021).
27. Aslam A. A., Schwendike J., Peatman S. C., Matthews A. J., Birch C. E., Bollasina M. A., Barrett P. A. & Azaneu M. V. C. Atmospheric Response to Mesoscale Ocean Eddies in the Maritime Continent. *J. Geophys. Res.: Atmos.* **130** (2025).
28. Cabrera M., Santini M., Lima L., Carvalho J., Rosa E., Rodrigues C. & Pezzi L. The southwestern Atlantic Ocean mesoscale eddies: A review of their role in the air-sea interaction processes. *J. Mar. Syst.* **235** (2022).
29. Laurindo L. C., Small R. J., Thompson L., Siqueira L., Bryan F. O., Chang P., Danabasoglu G., Kamenkovich I. V., Kirtman B. P., Wang H. & Zhang S. Role of Ocean and Atmosphere Variability in Scale‐Dependent Thermodynamic Air‐Sea Interactions. *J. Geophys. Res.: Oceans* **127** (2022).
30. Sun X. & Wu R. Spatial scale dependence of the relationship between turbulent surface heat flux and SST. *Clim. Dyn.* **58**, 1127-1145 (2021).
31. Jing Z., Fox-Kemper B., Cao H., Zheng R. & Du Y. Submesoscale Fronts and Their Dynamical Processes Associated with Symmetric Instability in the Northwest Pacific Subtropical Ocean. *J. Phys. Oceanogr.* **51**, 83-100 (2021).
32. McWilliams J. C. Submesoscale currents in the ocean. *Proc Math Phys Eng Sci* **472**, 20160117 (2016).
33. Zhang Z., Wang W. & Qiu B. Oceanic mass transport by mesoscale eddies. *Science* **345**, 322-324 (2013).
34. Cai W., Santoso A., Collins M., Dewitte B., Karamperidou C., Kug J.-S., Lengaigne M., McPhaden M. J., Stuecker M. F., Taschetto A. S., Timmermann A., Wu L., Yeh S.-W., Wang G., Ng B., Jia F., Yang Y., Ying J., Zheng X.-T., Bayr T., Brown J. R., Capotondi A., Cobb K. M., Gan B., Geng T., Ham Y.-G., Jin F.-F., Jo H.-S., Li X., Lin X., McGregor S., Park J.-H., Stein K., Yang K., Zhang L. & Zhong W. Changing El Niño–Southern Oscillation in a warming climate. *Nature Reviews Earth & Environment* **2**, 628-644 (2021).
35. Johnson G. C., McPhaden M. J., Rowe G. D. & McTaggart K. E. Upper equatorial Pacific Ocean current and salinity variability during the 1996–1998 El Niño–La Niña cycle. *J. Geophys. Res.: Oceans* **105**, 1037-1053 (2000).
36. McPhaden M. J. The child prodigy of 1997–98. *Nature* **398**, 599-561 (1999).
37. Chen T. & Guestrin C. Xgboost A scalable tree boosting system. *Proceedings of the 22nd ACM SIGKDD International Conference on Knowledge Discovery and Data Mining (KDD '16)*, 785–794 (2016).
38. Lundberg S. M., Erion G., Chen H., DeGrave A., Prutkin J. M., Nair B., Katz R., Himmelfarb J., Bansal N. & Lee S. I. From Local Explanations to Global Understanding with Explainable AI for Trees. *Nat Mach Intell* **2**, 56-67 (2020).
39. Lundberg S. M. & Lee S.-I. A unified approach to interpreting model predictions.

Advances in Neural Information Processing Systems **30**, 4765–4774 (2017).
40. Beron-Vera F. J. & Olascoaga M. J. An Assessment of the Importance of Chaotic Stirring and Turbulent Mixing on the West Florida Shelf. *J Phys Oceanogr* **39**, 1743-1755 (2009).
41. Liu Y., Wilson C., Green M. A. & Hughes C. W. Gulf Stream Transport and Mixing Processes via Coherent Structure Dynamics. *J. Geophys. Res.: Oceans* **123**, 3014-3037 (2018).
42. Zhan P., Guo D., Krokos G., Dong J., Duran R. & Hoteit I. Submesoscale Processes in the Upper Red Sea. *J. Geophys. Res.: Oceans* **127** (2022).
43. Frankignoul C. & Kestenare E. The surface heat flux feedback. Part I: estimates from observations in the Atlantic and the North Pacific. *Clim. Dyn.* **19**, 633-647 (2002).
44. Wang Z., Jing Z. & Song F. Weakened large-scale surface heat flux feedback at midlatitudes under global warming. *Nat Commun* **15**, 10020 (2024).
45. Dong C., Liu L., Nencioli F., Bethel B. J., Liu Y., Xu G., Ma J., Ji J., Sun W., Shan H., Lin X. & Zou B. The near-global ocean mesoscale eddy atmospheric-oceanic-biological interaction observational dataset. *Sci Data* **9**, 436 (2022).
46. Nencioli F., Dong C., Dickey T., Washburn L. & McWilliams J. C. A Vector Geometry–Based Eddy Detection Algorithm and Its Application to a High-Resolution Numerical Model Product and High-Frequency Radar Surface Velocities in the Southern California Bight. *J. Atmos. Oceanic Technol.* **27**, 564-579 (2010).
47. Huang B., Liu C., Banzon V., Freeman E., Graham G., Hankins B., Smith T. & Zhang H.-M. Improvements of the Daily Optimum Interpolation Sea Surface Temperature (DOISST) Version 2.1. *J. Clim.* **34**, 2923-2939 (2021).
48. Schlax M. G., Casey K. S., Chelton D. B., Liu C., Smith T. M. & Reynolds R. W. Daily High-Resolution-Blended Analyses for Sea Surface Temperature. *J. Clim.* **20**, 5473-5496 (2007).
49. Holte J., Talley L. D., Gilson J. & Roemmich D. An Argo mixed layer climatology and database. *Geophys. Res. Lett.* **44**, 5618-5626 (2017).
50. Haller G. Lagrangian Coherent Structures. *Annu. Rev. Fluid Mech.* **47**, 137-162 (2015).
51. Cui H., Tang D., Foltz G. R., Mei W., Liu H., Hoteit I., Li C., Zhang H., Sui Y. & Gu X. Drivers of Tropical Cyclone‐Induced Ocean Cooling in Different Seasons Over the Northwest Pacific From Explainable Machine Learning. *J. Geophys. Res.: Mach. Learn. Comput.* **2** (2025).
52. Cui H., Tang D., Liu H., Liu H., Sui Y., Lai Y. & Gu X. Modeling Ocean Cooling Induced by Tropical Cyclone Wind Pump Using Explainable Machine Learning Framework. *IEEE Trans. Geosci. Remote Sens.* **62**, 1-17 (2024).
53. Qin L., Zhu L., Liu B., Li Z., Tian Y., Mitchell G., Shen S., Xu W. & Chen J. Global expansion of tropical cyclone precipitation footprint. *Nat Commun* **15**, 4824 (2024).
54. Reichstein M., Camps-Valls G., Stevens B., Jung M., Denzler J., Carvalhais N.

& Prabhat. Deep learning and process understanding for data-driven Earth system science. *Nature* **566**, 195-204 (2019).

Supplementary Files

This is a list of supplementary files associated with this preprint. Click to download.

- Supplementaryinformation.docx